Porous lanthanide metal–organic frameworks with metallic conductivity

Grigorii Skorupskii[a], Khoa N. Le[b], Dmitri Leo Mesoza Cordova[c], Luming Yang[a], Tianyang Chen[a], Christopher H. Hendon[b], Maxx Q. Arguilla[c], and Mircea Dincă[a,1]

Metallic charge transport and porosity appear almost mutually exclusive. Whereas metals demand large numbers of free carriers and must have minimal impurities and lattice vibrations to avoid charge scattering, the voids in porous materials limit the carrier concentration, provide ample space for impurities, and create more charge-scattering vibrations due to the size and flexibility of the lattice. No microporous material has been conclusively shown to behave as a metal. Here, we demonstrate that single crystals of the porous metal–organic framework $Ln_{1.5}$(2,3,6,7,10,11-hexaoxytriphenylene) (Ln = La, Nd) are metallic. The materials display the highest room-temperature conductivities of all porous materials, reaching values above 1,000 S/cm. Single crystals of the compounds additionally show clear temperature-deactivated charge transport, a hallmark of a metallic material. Lastly, a structural transition consistent with charge density wave ordering, present only in metals and rare in any materials, provides additional conclusive proof of the metallic nature of the materials. Our results provide an example of a metal with porosity intrinsic to its structure. We anticipate that the combination of porosity and chemical tunability that these materials possess will provide a unique handle toward controlling the unconventional states that lie within them, such as charge density waves that we observed, or perhaps superconductivity.

Metal–organic frameworks | electrical transport | charge density wave | low-dimensional materials

Significance

No reported material both is intrinsically porous and conducts electricity like a metal. This incompatibility appears to be rooted in the fundamental mechanisms responsible for metallic charge transport. Here, we identified one class of materials, namely, metal–organic frameworks, to be well-suited for the search of intrinsically porous metals. The porous framework $Ln_{1.5}$(2,3,6,7,10,11-hexaoxytriphenylene) (Ln = La, Nd) is metallic, as seen from electrical conductivity measurements and theoretical calculations. As additional proof, this system hosts a state exclusive to metals known as a charge density wave. We believe that this combination of properties will serve as an important milestone in the study of unconventional conductors and provide a flexible platform for the study of more complex physics in metal–organic frameworks.

Porosity and metallic charge transport rarely coexist. The defining characteristic of a metal is an inverse relationship between its electrical conductivity and temperature. This is due to scattering; the mobility of charge carriers is lowered when they interact with, or scatter off of, impurities or lattice vibrations (i.e., phonons)—which themselves intensify with temperature (1). In porous materials, scattering processes are further intensified by the presence of physical voids, which also reduce the charge carrier concentration; typically larger unit cells, which provide additional high-amplitude vibrations; and higher concentrations of defects and impurities. Despite its seemingly antithetical nature, the combination of electrical conductivity and porosity is critical for a variety of applications, such as charge storage (2) or electrocatalysis (3). Materials that show both of these features are extremely rare, with activated carbons (4) or holey graphenes (5) overwhelmingly represented in the literature. They, however, are not metallic and are not easily tunable chemically. One set of porous materials that provides a wide range of chemical tunability is metal–organic frameworks (MOFs).

MOFs are generally insulating because they lack efficient pathways for charge transport. First, their lattices are generally ionic, meaning the linkages between the constituent organic ligands and the metal nodes create localized electronic states and impede charge delocalization. Second, the contents of the pores, namely, solvent molecules, inert gas, or vacuum, are themselves insulating (6). Despite these challenges, several recent reports show that electrical conductivity can exist in certain types of MOFs, especially when the ligands enable strong charge delocalization (7–9). Frameworks built with triphenylene- and benzene-based ligands stand out in this sense because these flat aromatic linkers form strongly delocalized orbitals with the metal ions and have a strong propensity for π–π stacking, combining the defining features of traditional inorganic and organic conductors (7, 8, 10). Indeed, a dense coordination polymer with these features, Cu_3(benzenehexathiol) (11), is metallic, shows high room-temperature conductivity of 2,500 S/cm, and even becomes superconducting at ultralow temperatures. For porous MOFs, triphenylene-based materials show the highest conductivities, on the level of 100 S/cm (12), which is comparable to graphite. However, even though some porous MOFs are computationally predicted to be metallic, there is only circumstantial evidence confirming their metallic nature. At best, this behavior coexists with and is overwhelmed by much clearer signs of semiconductor behavior (7, 13–16).

Here, we report that high-quality single crystals of Ln$_{1.5}$(2,3, 6,7,10,11-hexaoxytriphenylene) (Ln$_{1.5}$HOTP; Ln = La, Nd) demonstrate clear temperature-deactivated—metallic—conductivity. They further demonstrate the highest room-temperature electrical conductivity among all MOFs or any other intrinsically porous material, reaching values above 1,000 S/cm. As a unique and rare signature of one-dimensional metals, the materials also undergo an incommensurate ordering transition consistent with the formation of a charge density wave (CDW) state. The latter is possible only in metallic materials and has never been observed for an MOF or any other porous material. The CDW transition temperature, namely, 360 K to 375 K, is the highest for any organic-based material. The MOFs crystallize under easily accessible synthetic conditions from commercially available precursors, thus providing a convenient and tunable platform for studying the complex physics arising from the combination of the metallic charge transport and porosity.

Results and Discussion

Under conditions mimicking those reported previously (10) for the cation-deficient isostructural analogs Ln$_{1.5-x}$HOTP ($x = 0.2$ to 0.3), H$_6$HOTP reacts with a large excess of Ln(NO$_3$)$_3$ to produce dark blue/purple, highly reflective, needle-shaped crystals of Ln$_{1.5}$HOTP (Fig. 1E). Important synthetic deviations from the previous report include 1) performing the reaction under an N$_2$ atmosphere to prevent overoxidation of the linker and related cation deficiency; 2) using N,N-dimethylacetamide as a solvent, as its hydrolysis produces the base that deprotonates the linker in situ; and 3) considerably increasing the reaction temperature to 135 °C to enable a more reversible metal–ligand bond formation. Altogether, these modifications produced significantly larger crystals of the desired materials, thereby enabling the critical single-crystal experiments underlying this study.

Single-crystal X-ray diffraction data collected above 375 K show that both frameworks crystallize in monoclinic systems (space group P2$_1$/n for La$_{1.5}$HOTP and C2/c for Nd$_{1.5}$HOTP). A portion of the crystal structure of La$_{1.5}$HOTP at 375 K (Fig. 1), essentially identical to that of Nd$_{1.5}$HOTP and in good agreement to the model advanced previously from powder diffraction studies, shows columns of closely stacked HOTP linkers connected into a honeycomb net by eight-coordinate square–antiprismatic lanthanide ions. The apparent hexagonal symmetry of both structures is broken by only 10% of the metal sites, which deviate from their idealized position and lead to heavy twinning.

Computed electronic band structures (EBSs) of Ln$_{1.5}$HOTP, obtained by density functional theory (DFT) calculations (Fig. 2 A and B), show that the materials possess electronic bands that resemble one-dimensional metals, with disperse bands crossing the Fermi level along the A-Γ vector and relatively flat bands along other vectors, consistent with data previously found for Ln$_{1.5-x}$HOTP (10). La$_{1.5}$HOTP and Nd$_{1.5}$HOTP are qualitatively similar electronically, except for additional bands brought by the partially filled $4f$ orbitals of Nd^{3+}. The strong electronic anisotropy evidenced in the band diagrams is justified by considering the covalent and noncovalent interactions within the material; the Ln–O bonds that provide connectivity within the honeycomb layers are highly ionic (17), allow only negligible charge delocalization, and thus give rise to flat bands along the Γ-K-M directions, where the Fermi level lies within a gap. However, the structure features extensive π–π stacking in one dimension along the crystallographic c direction, where the particularly short stacking distance between neighboring organic linkers enables an efficient pathway for charge delocalization and formation of disperse bands.

Optical properties of the materials allow direct confirmation of the electronic anisotropy. Visible to near-infrared absorbance spectra of single crystals of Ln$_{1.5}$HOTP (Fig. 2C) measured orthogonal to the c direction reveal an absorption maximum around 2.1 to 2.3 eV. Along the c direction, the absorption gets considerably broader and the maximum falls below 2 eV in both compounds. Broadening and red-shifting of the absorption
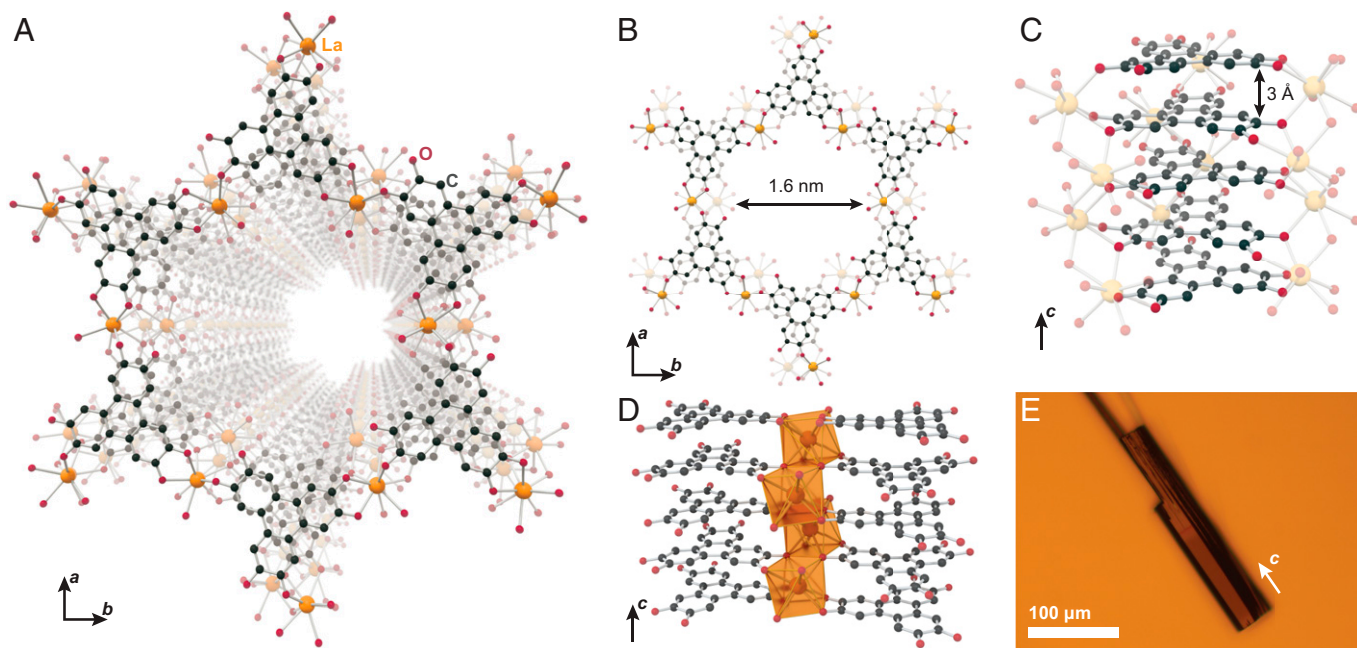

Fig. 1. Crystal structure of La$_{1.5}$HOTP. (*A–D*) The structure features large accessible one-dimensional channels (*A*), formed inside honeycomb-like layers (*B*) of the trigonal HOTP linkers connected by continuous –La–O– chains, with the La^{3+} ions in square antiprismatic environment (*D*). The structure features extensive π–π stacking interactions between the linkers, which are separated by only 3.0 Å at room temperature (*C*). (*E*) The material forms dark-blue or purple hexagonal needles, with the crystallographic c direction, which is collinear to π–π stacking in the material, aligned along the longer dimension of the crystals. In the models, orange shows lanthanum, red shows oxygen, and dark gray shows carbon. Hydrogen atoms, minority disorder components, and uncoordinated solvent molecules were omitted for clarity.
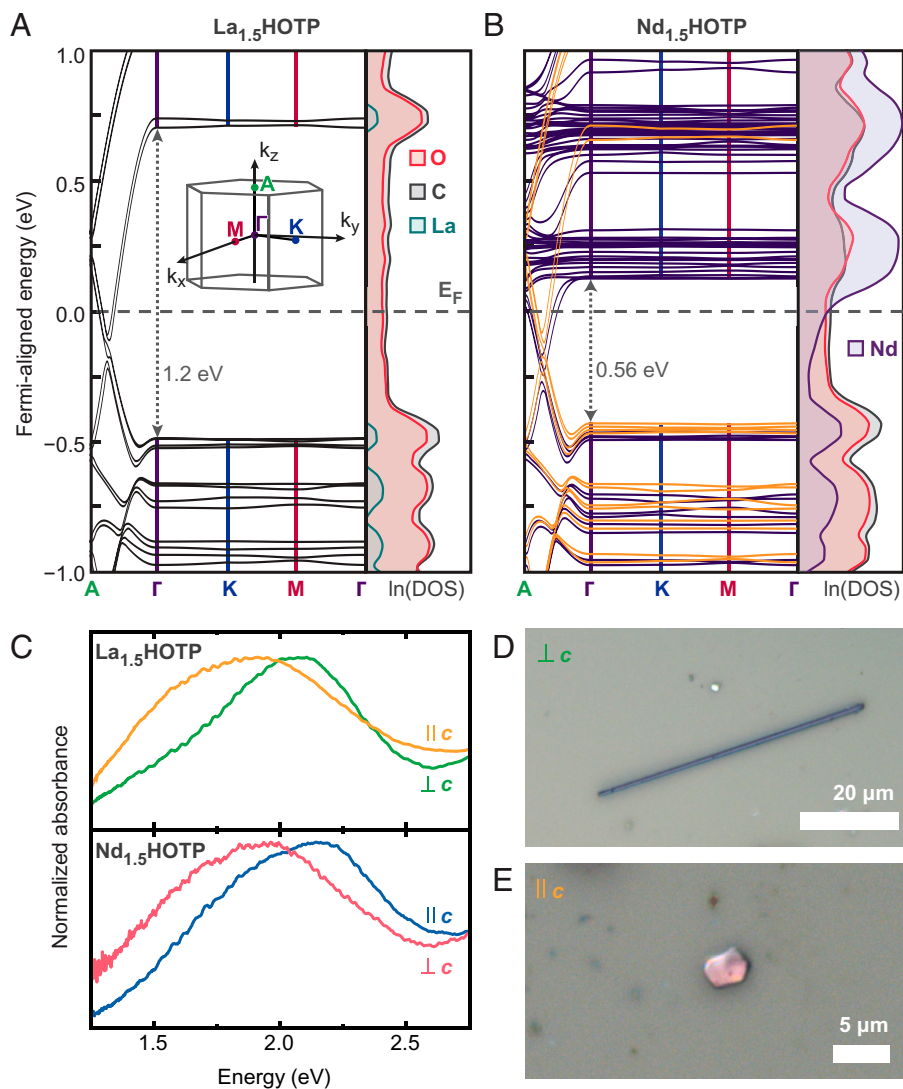
Fig. 2. Electronic structure of $Ln_{1.5}HOTP$. (*A* and *B*) From DFT calculations, both $La_{1.5}HOTP$ (*A*) and $Nd_{1.5}HOTP$ (*B*) are metals, with considerable dispersion along the A-Γ direction originating from the strong π–π stacking interactions, and essentially flat bands along Γ-K-M. The addition of the partially occupied 4f orbitals of Nd^{3+} causes $Nd_{1.5}HOTP$ to have a ferromagnetic ground state ((*B*) shows different spin bands with different colors) and adds a significant number of flat, mostly Nd-originated bands above the Fermi level. The band structure plots are supplemented with projected density of states (DOS) plots, showing the relative contribution of each element to the band structure. (*C*) Optical transmission measurements, performed on cleaved microscopic crystals of both materials, qualitatively agree with the calculated band structures; when measured along the *c* direction, the crystals show significantly broader and red-shifted absorption features than when measured along the *ab* planes. (*D* and *E*) Examples of the crystals used for the measurements presented on *C*.

features can readily be correlated with an increase in the density of states (DOSs) across the continuum of energy states along the A-Γ vector, compared to the semiconducting gap in the honeycomb plane.

Four-probe single-crystal electrical transport devices (Fig. 3 *D* and *E* and *SI Appendix*, Fig. S3) provided clear confirmation of the metallic behavior predicted by DFT. At room temperature, both $La_{1.5}HOTP$ and $Nd_{1.5}HOTP$ showed device-dependent electrical conductivities reaching 900 S/cm and 1,080 S/cm, respectively (Fig. 3*A*). These values are six orders of magnitude higher than the conductivities reported (10) for cation-deficient $Ln_{1.5-x}HOTP$, although the latter had only been measured as polycrystalline pressed pellets, where grain boundaries likely increase resistivity. Notably, these values considerably surpass the previous record of electrical conductivity in porous MOFs, namely, 150 S/cm shown by $Ni_3(2,3,6,7,10,11$-hexaiminotriphenylene$)_2$ (12). In fact, to our knowledge, this is also the highest electrical conductivity shown by any porous material reported to date. Crystals of $Nd_{1.5}HOTP$

further show temperature-deactivated conductivity dependence between 250 and 350 K (fragility of the thin crystals precluded measurements outside this range), a clear characteristic of metallic behavior.

Intriguingly, single-crystal diffraction data revealed that, below 370 K, both $La_{1.5}HOTP$ and $Nd_{1.5}HOTP$ give rise to additional satellite reflection peaks, which are consistent with incommensurate modulation (18) (Fig. 4 *A–C*). In modulated crystals, the translational symmetry of the parent structure is broken by the introduction of a periodic modulation whose direction and periodicity are defined by a modulation wavevector. When this wavevector can be represented as a linear combination of the lattice vectors with rational coefficients, the modulation is said to be commensurate, and commensurately modulated structures can always be described by (sometimes very large) supercells of the original structure. When the wavevector demands an irrational number of the original lattice vectors, the structure is said to be incommensurately modulated and cannot be represented with any three-dimensional cell. Below 370 K, both $La_{1.5}HOTP$ and
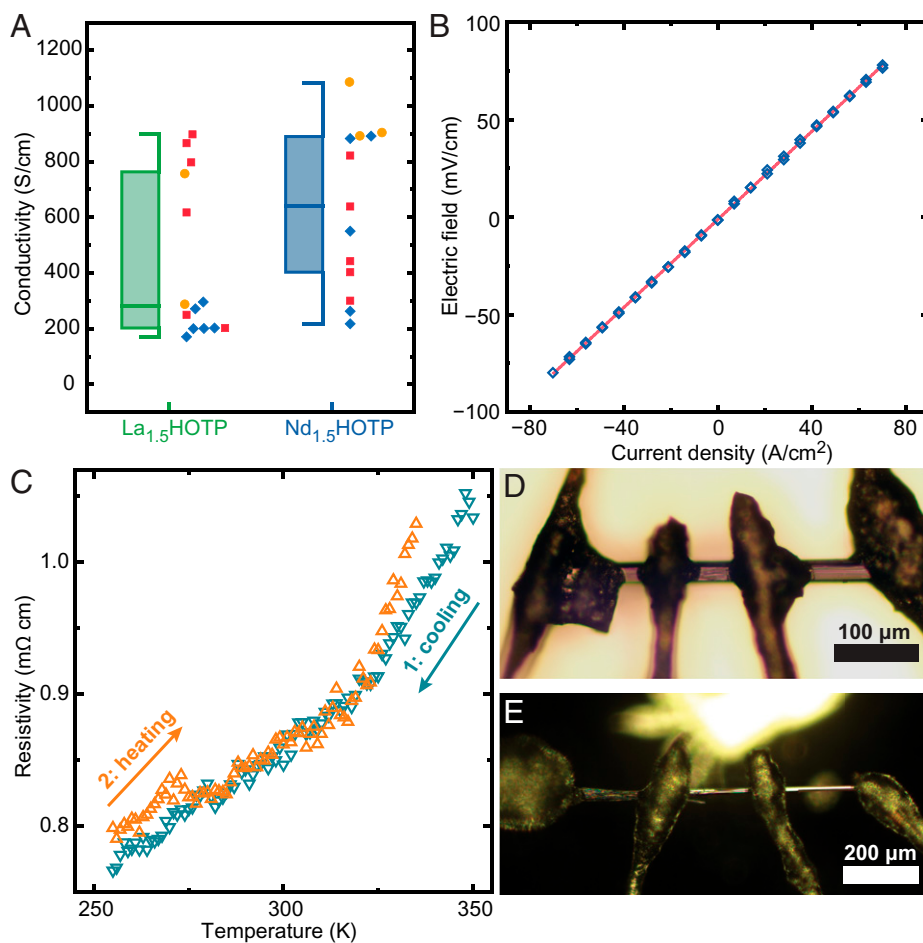
Fig. 3. Electrical transport properties of $Ln_{1.5}HOTP$. (*A*) Both $Ln_{1.5}HOTP$ materials showed comparable room-temperature electrical conductivity values, ranging between 170 and 1,080 S/cm, which is considerably higher than the previous record of 150 S/cm, shown by $Ni_3(2,3,6,7,10,11\text{-hexaiminotriphenylene})_2$ (12). (*B*) The conductivity devices showed linear voltage characteristics in a wide range (red line shows linear fit of the data, $R^2 = 0.999$). (*C*) Between 250 and 350 K, $Nd_{1.5}HOTP$ showed clear temperature-deactivated conductivity. Devices were fragile and fractured outside this temperature range. (*D*) Typical variable-temperature device under a bright-field optical microscope. (*E*) Typical device used for room-temperature measurements under a dark-field optical microscope. Box chart in *A* uses 25 to 75% limits for the boxes, minimum and maximum for the whiskers, and median value for the center line. Each symbol in *A* denotes a single-crystal device, with symbols and colors denoting different batches.

$Nd_{1.5}HOTP$ can be indexed in a monoclinic cell of the same parameters as the nonmodulated, high-temperature phases but require an incommensurate modulation vector along the *c* direction of $\sim 0.23c^*$ to $0.28c^*$, depending on the specific batch and material.

Raman spectra of single crystals of $Ln_{1.5}HOTP$ (Fig. 4 *D* and *E*) also exhibit anomalous features at the same transition temperature of ~ 363 to 368 K. Specifically, we observe clear discontinuities close to the incommensurate transition temperature in the Raman shifts and intensities of several bands, associated with the highly anisotropic triphenylene core vibrational modes perpendicular to the crystallographic *c* axis (19). These may signify a redistribution of charges within the linker and the framework. Importantly, both X-ray and Raman data convey that the structural transition at ~ 370 K is fully reversible and occurs regardless of the solvation state of either material. Incommensurate modulation is rare in MOFs (18) and so far has only been reported as a guest solvent-dependent phenomenon in electrically insulating systems (20, 21), never intrinsic to the framework skeleton. In molecular materials, incommensurate modulation often occurs due to a complex interplay of steric effects and noncovalent interactions (18). In our case, however, evidence suggests that this ordering has an electronic origin.

One-dimensional metals are generally unstable and prone to Peierls distortions. Although a Peierls distortion of an ideal

single-atom chain with one electron per atom strictly doubles the unit cell, in the more general case, the Peierls instability leads to the formation of an incommensurately modulated structure known as a CDW (22). The one-dimensional metallic ground state coupled with the temperature-induced formation of an incommensurate superlattice provide strong evidence for assigning the structural transition in $Ln_{1.5}HOTP$ to CDW ordering.

A signature of CDW materials is the characteristic Bardeen–Cooper–Schreiffer (BCS)-like temperature dependence of the energy gap opened by the Peierls transition. This energy gap serves as the order parameter in a CDW system and is proportional to the square root of the satellite reflection intensities (22, 23). Importantly, the intensities of the superlattice reflections (I_{sat}) in both $Ln_{1.5}HOTP$ materials are fit well by a BCS-like dependence (Fig. 4*C*) (here, the fit employs the commonly used gap interpolation formula $\Delta \sim tanh(k\sqrt{1 - T/T_c})$ (24–26), where Δ is the gap width, T is the temperature, T_c is the critical temperature where the transition happens, and k is a refined constant). Additional confirmation of our assigning the transition as CDW ordering comes from the behavior of the intensities of I_{sat} near the transition temperature. These follow a polynomial law $\sqrt{I_{sat}} \sim (1 - T/T_c)^\beta$, where β is the critical exponent (27). The fitting (*SI Appendix*, Fig. S4) provides critical temperatures $T_c = 361$ K for $La_{1.5}HOTP$ and $T_c = 365$ K for $Nd_{1.5}HOTP$,
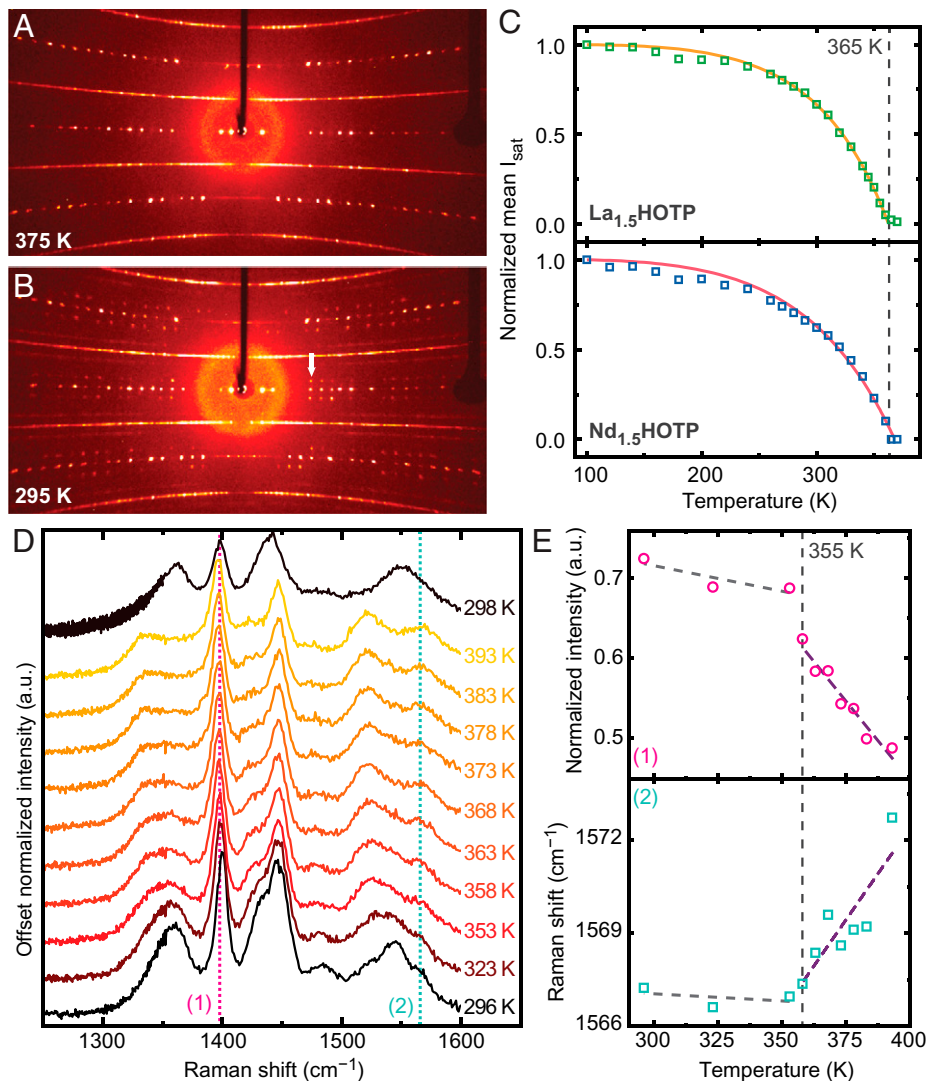
Fig. 4. CDW transition in $Ln_{1.5}HOTP$. (*A*) High-temperature (above 300 to 375 K) diffraction data for both materials (here, showing $Nd_{1.5}HOTP$) are fit well by a twinned monoclinic cell, albeit with considerable diffuse scattering. (*B*) Below the incommensurate transition temperature, both $Ln_{1.5}HOTP$ develop bright satellite reflections (highlighted by the white arrow) that cannot be indexed in any three-dimensional cell. (*C*) The intensities of the satellite reflections follow a BCS-type dependence; intensities scale with the square of the CDW gap, Δ, and its dependence with temperature was calculated using the gap interpolation formula $\Delta \sim tanh(k\sqrt{1-T/T_c})$, where k is a refined constant. Solid lines show fit to this dependence and markers show data. (*D*) Temperature-dependent Raman spectra of $Nd_{1.5}HOTP$ measured with excitation light polarized along the crystallographic c axis possess clear anomalies at the incommensurate transition temperature (350 to 360 K). Most prominent are anomalies related to the strong Raman bands in the 1,100- to 1,600-cm^{-1} range, originating from vibrations within the triphenylene core of the linker. (*E*) Clear discontinuities can be seen in the intensity (*Top*) and Raman shift (*Bottom*) of two bands, indicated with pink and teal dotted lines in *D*. The dashed grey vertical lines in panels C and E highlight the discontinuities, attributed to CDW order, in the satellite reflection intensity, I_{sat}, fitting and temperature-dependent Raman intensities and shifts of select phonon modes originating from the triphenylene core. Additional Raman data are provided in *SI Appendix*, Figs. S5–S9. Evidently, a change in the phononic structure of the material occurs at 350 to 360 K.

with the same critical exponent of $\beta = 1/3$, as expected for a second-order transition in the presence of fluctuations (28). This analysis proves that square root satellite intensities behave as a real order parameter in the $Ln_{1.5}HOTP$ systems, which is characteristic of CDW materials (22). Relevantly, a number of other CDW materials exhibit similar critical behavior (27, 29), including the well-established example of "blue bronze" $K_{0.3}MoO_3$ (30). Importantly, only a limited set of materials has been conclusively proven to host CDW states, most prominently organic charge-transfer salts (31) and low-dimensional metal chalcogenides and oxides (32–35). We emphasize that CDW ordering necessarily originates in metallic systems. This, together with the record-setting room-temperature conductivity, temperature-deactivated transport, and DFT calculations, provides conclusive proof of the metallic nature of $Ln_{1.5}HOTP$.

The foregoing results demonstrate metallic conductivity with clear temperature-deactivated transport for $Ln_{1.5}HOTP$.

The room-temperature conductivity of $Nd_{1.5}HOTP$ exceeds 1,000 S/cm and is highest among all porous materials. The presence of a CDW transition, exclusively observed in metallic compounds, further substantiates the metallic behavior of the MOFs and points to other potential exotic physical states in these materials. Indeed, we believe, and theoretical studies corroborate (36–40), that other physical phenomena lie undiscovered in these materials—including, perhaps, exotic quantum states and superconductivity. Low-temperature or high-pressure measurements may lead to the discovery of further anomalies even within the $Ln_{1.5}HOTP$ series.

Materials and Methods

Typical Synthesis of $Ln_{1.5}HOTP$ (Ln = La, Nd). In an N_2-filled glove box, 19.5 mg H_6HOTP (0.060 mmol, 1 equiv) was dissolved in 0.7 mL *N,N*-dimethylacetamide with heating to 90 °C to produce a yellow solution (blue in

the case of H_6HOTP produced in-house). Then, 4,156.9 mg of $La(NO_3)_3 \cdot 6\,H_2O$ or 4,208.1 mg of $Nd(NO_3)_3 \cdot 6\,H_2O$ (9.600 mmol, 160 equiv) was dissolved in 6 mL of deoxygenated water by heating to 90 °C. The linker solution was then combined with the solution of the metal salt to produce a pale yellow (La) or pink (Nd) solution, which was then passed through a 200-nm polyethersulfone filter and transferred into a 35 mL-capacity glass pressure tube (Synthware). For improved crystallinity and yield, borosilicate glass rods were sanded with 220-grit sandpaper, cleaned by sonication in water and methanol, and added to the reaction mixture in order to provide nucleation sites for the crystals. The pressure tube was then fitted with a polytetrafluoroethylene screw plug with a back-seal silicone O-ring (Synthware), taped with electrical tape (3M), and placed inside a preheated oven set to 135 °C. The mixture was kept at that temperature for 72 h and was allowed to cool down to room temperature over 8 h. The tube was then transferred into a N_2-filled glove box, where it was opened, and the reaction was worked up by removing the solution using a pipette and transferring the crystals into deoxygenated water. The crystals were washed by soaking in deoxygenated water four times with at least one 24-h soak, and no soaks shorter than 1 h. The crystals were then similarly soaked in deoxygenated methanol and, in some cases, in dichloromethane or diethyl ether. The crystals can be stored in air under methanol, dichloromethane, or diethyl ether without observed changes in crystal quality or electrical conductivity over the course of at least several months.

Single-Crystal X-Ray Diffraction. Single-crystal diffraction data were collected on a Bruker-AXS D8 Venture Kappa Duo diffractometer coupled to a Photon III charge-integrating pixel array detector using Mo Kα radiation ($\lambda = 0.71073$ Å) from an IμS 3.0 microfocus source, performing φ-and ω-scans. Patterns were integrated with SAINT (Bruker-AXS) and scaled with SADABS (Bruker-AXS) and then processed using either the SHELX suite (41) or JANA2020 (42). Further details are provided in *SI Appendix*.

Electrical Conductivity Measurements. Electrical conductivity measurements were performed in the linear four-contact probe configuration (43) on devices fabricated using copper or gold wires and water-based graphite conductive adhesive (EMS). A Janis ST-500 probe station coupled to a Keithley 2450 sourcemeter was used for room-temperature measurements, and a Quantum Design Physical Property Measurement System (PPMS) Dynacool 9 T, equipped with the Electrical Transport Option, was used for variable-temperature measurements. Conductivity measurements on pressed pellet-based devices in the van der Pauw configuration were also initially attempted but yielded conductivities at least four orders of magnitude lower, likely due to the overwhelming influence of grain boundary resistance. Further detail on single-crystal device fabrication and measurement is provided in *SI Appendix*.

DFT Calculations. DFT calculations were carried out using the Vienna ab initio Simulation Package (version 5.4.4) (44). All structures were first equilibrated using the unrestricted GGA-PBEsol exchange-correlation functional (45), and then single-point calculations were performed on these structures with the same functional to obtain the initial wavefunctions for the EBS and DOS calculations. The same functional was finally used to obtain the EBS and DOS for $La_{1.5}HOTP$, whereas for $Nd_{1.5}HOTP$ the GGA+U functional was used to properly account for the interactions of 4f electrons (46). Further detail is provided in *SI Appendix*.

Optical Spectroscopy. Visible to near-infrared range optical measurements of $La_{1.5}HOTP$ and $Nd_{1.5}HOTP$ single crystals were carried out using a Cytoviva hyperspectral imaging microscope system equipped with an ImSpector V10E spectrograph, spectral camera, and L1090 MR16 150W Halogen light source. Bright-field transmission spectroscopy measurements were performed on in-plane (incident light orthogonal to the c axis)–oriented and out-of-plane (incident light parallel to the c axis)–oriented $La_{1.5}HOTP$ and $Nd_{1.5}HOTP$ crystals mounted on double-sided polished 500-μm-thick Z-cut quartz substrates (University Wafers). Background correction of the transmission hyperspectral micrographs was performed by subtracting the light source and quartz substrate contributions. Background correction, conversion to absorbance units, region of interest averaging, and spectra extraction were performed on raw hyperspectral micrographs using the L3HARRIS ENVI data processing software.

Raman Spectroscopy. Temperature-dependent Raman spectra were collected on in-plane (incident laser orthogonal to the c axis)–oriented and out-of-plane (incident laser parallel to the c axis)–oriented $La_{1.5}HOTP$ and $Nd_{1.5}HOTP$ single crystals using a Renishaw Invia Raman microscope equipped with a charge-coupled detector capable of measurements up to 1-cm^{-1} resolution. In these measurements, the crystals were mounted onto Si/SiO_2 (300 nm) substrates with fiduciary markers. A 532-nm laser was employed as the illumination source with a nominal power of 0.22 mW and 10 s of exposure time. The sample temperature was controlled using a Linkam THMS600 stage purged with pure Ar gas. Raw intensities were normalized, and pertinent sections of the Raman spectra were fit with a cubic spline background and Lorentzian peaks with MagicPlotPro 2.9 software. To compare temperature-dependent behavior of specific vibrational modes, the peak amplitude was used as a measure of intensity and the peak center as a measure of position. The out-of-plane (c-axis) crystal orientation was identified from large flat crystal facets, while the in-plane crystal (ab-plane) crystal orientation was identified from domains of hexagonal platelets.

Author affiliations: [a]Department of Chemistry, Massachusetts Institute of Technology, Cambridge, MA, 02139; [b]Department of Chemistry and Biochemistry, University of Oregon, Eugene, OR, 97403; and [c]Department of Chemistry, University of California, Irvine, Irvine, CA, 92697

1. C. Kittel, *Introduction to Solid State Physics* (Wiley, 2004).
2. D. Sheberla et al., Conductive MOF electrodes for stable supercapacitors with high areal capacitance. *Nat. Mater.* **16**, 220–224 (2017).
3. E. M. Miner, L. Wang, M. Dincă, Modular O_2 electroreduction activity in triphenylene-based metal-organic frameworks. *Chem. Sci. (Camb.)* **9**, 6286–6291 (2018).
4. C. Liu, F. Li, L.-P. Ma, H.-M. Cheng, Advanced materials for energy storage. *Adv. Mater.* **22**, E28–E62 (2010).
5. M. F. El-Kady, V. Strong, S. Dubin, R. B. Kaner, Laser scribing of high-performance and flexible graphene-based electrochemical capacitors. *Science* **335**, 1326–1330 (2012).
6. L. S. Xie, G. Skorupskii, M. Dincă, Electrically conductive metal-organic frameworks. *Chem. Rev.* **120**, 8536–8580 (2020).
7. D. Sheberla et al., High electrical conductivity in Ni₃(2,3,6,7,10,11-hexaiminotriphenylene)₂, a semiconducting metal-organic graphene analogue. *J. Am. Chem. Soc.* **136**, 8859–8862 (2014).
8. T. Kambe et al., π-Conjugated nickel bis(dithiolene) complex nanosheet. *J. Am. Chem. Soc.* **135**, 2462–2465 (2013).
9. R. Dong et al., High-mobility band-like charge transport in a semiconducting two-dimensional metal-organic framework. *Nat. Mater.* **17**, 1027–1032 (2018).
10. G. Skorupskii et al., Efficient and tunable one-dimensional charge transport in layered lanthanide metal-organic frameworks. *Nat. Chem.* **12**, 131–136 (2020).
11. X. Huang et al., Superconductivity in a copper(II) coordination polymer with perfect kagome structure. *Angew. Chem. Int. Ed. Engl.* **57**, 146–150 (2018).
12. R. W. Day et al., Single crystals of electrically conductive two-dimensional metal-organic frameworks: Structural and electrical transport properties. *ACS Cent. Sci.* **5**, 1959–1964 (2019).
13. J. H. Dou et al., Signature of metallic behavior in the metal-organic frameworks M₃(hexaiminobenzene)₂ (M = Ni, Cu). *J. Am. Chem. Soc.* **139**, 13608–13611 (2017).
14. M. E. Foster, K. Sohlberg, M. D. Allendorf, A. A. Talin, Unraveling the semiconducting/metallic discrepancy in Ni₃(HITP)₂. *J. Phys. Chem. Lett.* **9**, 481–486 (2018).
15. A. J. Clough et al., Metallic conductivity in a two-dimensional cobalt dithiolene metal-organic framework. *J. Am. Chem. Soc.* **139**, 10863–10867 (2017).
16. A. J. Clough et al., Room temperature metallic conductivity in a metal-organic framework induced by oxidation. *J. Am. Chem. Soc.* **141**, 16323–16330 (2019).
17. S. A. Cotton, *Lanthanide and Actinide Chemistry* (John Wiley & Sons, Ltd, 2006).
18. J. J. Oppenheim, G. Skorupskii, M. Dincă, Aperiodic metal-organic frameworks. *Chem. Sci. (Camb.)* **11**, 11094–11103 (2020).

19. V. Schettino, Infrared and Raman spectra of crystalline triphenylene and triphenylene-d12 and normal coordinates calculations. *J. Mol. Spectrosc.* **34**, 78–96 (1970).
20. G. Chaplais *et al.*, IM-19: A new flexible microporous gallium based-MOF framework with pressure- and temperature-dependent openings. *Phys. Chem. Chem. Phys.* **11**, 5241–5245 (2009).
21. J. Li *et al.*, Guest-controlled incommensurate modulation in a meta-rigid metal-organic framework material. *J. Am. Chem. Soc.* **142**, 19189–19197 (2020).
22. G. Grüner, *Density Waves in Solids* (CRC Press, ed. 1, 1994).
23. G. Grüner, The dynamics of charge-density waves. *Rev. Mod. Phys.* **60**, 1129–1181 (1988).
24. K. Senapati, M. G. Blamire, Z. H. Barber, Spin-filter Josephson junctions. *Nat. Mater.* **10**, 849–852 (2011).
25. S. A. Sergeenkov, Electric field dependence of the thermal conductivity of a granular superconductor: Giant field-induced effects predicted. *JETP Lett.* **76**, 170–174 (2002).
26. F. Gross *et al.*, Anomalous temperature dependence of the magnetic field penetration depth in superconducting UBe_{13}. *Z. Phys. B Condens. Matter* **64**, 175–188 (1986).
27. P. Hofmann *et al.*, Strong-coupling charge density wave in a one-dimensional topological metal. *Phys. Rev. B* **99**, 035438 (2019).
28. T. Ma, S. Wang, *Phase Transition Dynamics* (Springer New York, 2014).
29. G. Brusdeylins *et al.*, He-atom scattering study of the temperature-dependent charge-density-wave surface structure and lattice dynamics of $2H-TaSe_2(001)$. *Phys. Rev. B Condens. Matter* **41**, 5707–5716 (1990).
30. S. Girault, A. H. Moudden, J. P. Pouget, Critical x-ray scattering at the Peierls transition of the blue bronze. *Phys. Rev. B Condens. Matter* **39**, 4430–4434 (1989).
31. D. Jérome, H. J. Schulz, Organic conductors and superconductors. *Adv. Phys.* **31**, 299–490 (1982).
32. G. Travaglini, P. Wachter, J. Marcus, C. Schlenker, The blue bronze $K_{0.3}MoO_3$: A new one-dimensional conductor. *Solid State Commun.* **37**, 599–603 (1981).
33. J. A. Wilson, F. J. Di Salvo, S. Mahajan, Charge-density waves and superlattices in the metallic layered transition metal dichalcogenides. *Adv. Phys.* **24**, 117–201 (1975).
34. R. M. Fleming, C. C. Grimes, Sliding-mode conductivity in $NbSe_3$: Observation of a threshold electric field and conduction noise. *Phys. Rev. Lett.* **42**, 1423–1426 (1979).
35. A. Zettl *et al.*, Charge density wave transition and nonlinear conductivity in NbS_3. *Solid State Commun.* **43**, 345–347 (1982).
36. J. L. Mancuso, A. M. Mroz, K. N. Le, C. H. Hendon, Electronic structure modeling of metal-organic frameworks. *Chem. Rev.* **120**, 8641–8715 (2020).
37. M. Wu *et al.*, Conetronics in 2D metal-organic frameworks: Double/half Dirac cones and quantum anomalous Hall effect. *2D Mater.* **4**, 015015 (2017).
38. J. Li, R. Wu, Metal-organic frameworks: Possible new two-dimensional magnetic and topological materials. *Nanoscale* **12**, 23620–23625 (2020).
39. L. Z. Zhang *et al.*, Intrinsic two-dimensional organic topological insulators in metal-dicyanoanthracene lattices. *Nano Lett.* **16**, 2072–2075 (2016).
40. Z. F. Wang, N. Su, F. Liu, Prediction of a two-dimensional organic topological insulator. *Nano Lett.* **13**, 2842–2845 (2013).
41. G. M. Sheldrick, A short history of SHELX. *Acta Crystallogr. A* **64**, 112–122 (2008).
42. V. Petříček, M. Dušek, L. Palatinus, Crystallographic computing system JANA2006: General features. *Z. Kristallogr. Cryst. Mater.* **229**, 345–352 (2014).
43. L. Sun, S. S. Park, D. Sheberla, M. Dincă, Measuring and reporting electrical conductivity in metal-organic frameworks: $Cd_2(TTFTB)$ as a case study. *J. Am. Chem. Soc.* **138**, 14772–14782 (2016).
44. G. Kresse, J. Furthmüller, Efficient iterative schemes for ab initio total-energy calculations using a plane-wave basis set. *Phys. Rev. B Condens. Matter* **54**, 11169–11186 (1996).
45. J. P. Perdew *et al.*, Restoring the density-gradient expansion for exchange in solids and surfaces. *Phys. Rev. Lett.* **100**, 136406 (2008).
46. F. Nilsson, R. Sakuma, F. Aryasetiawan, Ab initio calculations of the Hubbard U for the early lanthanides using the constrained random-phase approximation. *Phys. Rev. B Condens. Matter Mater. Phys.* **88**, 125123 (2013).
47. G. Skorupskii *et al.*, Porous lanthanide metal–organic frameworks with metallic conductivity. Zenodo. https://zenodo.org/record/5278822#.YvBykHZBy3A. Deposited 1 August 2022.
48. G. Skorupskii *et al.*, Porous lanthanide metal–organic frameworks with metallic conductivity. Cambridge Structural Database. https://www.ccdc.cam.ac.uk/structures/Search?Ccdcid=2104596-2104597. Deposited 1 August 2022.